



UNIVERSITY OF LEEDS

This is a repository copy of *Magnetic properties of gas hydrate-bearing sediments and their association with iron geochemistry in the Sea of Marmara, Turkey*.

White Rose Research Online URL for this paper:

<https://eprints.whiterose.ac.uk/195486/>

Version: Accepted Version

Article:

Yang, H, Zhang, P, Lu, H et al. (6 more authors) (2023) Magnetic properties of gas hydrate-bearing sediments and their association with iron geochemistry in the Sea of Marmara, Turkey. *Chemical Geology*, 620. 121339. ISSN 0009-2541

<https://doi.org/10.1016/j.chemgeo.2023.121339>

© 2023, Elsevier. This manuscript version is made available under the CC-BY-NC-ND 4.0 license <http://creativecommons.org/licenses/by-nc-nd/4.0/>.

Reuse

This article is distributed under the terms of the Creative Commons Attribution-NonCommercial-NoDerivs (CC BY-NC-ND) licence. This licence only allows you to download this work and share it with others as long as you credit the authors, but you can't change the article in any way or use it commercially. More information and the full terms of the licence here: <https://creativecommons.org/licenses/>

Takedown

If you consider content in White Rose Research Online to be in breach of UK law, please notify us by emailing eprints@whiterose.ac.uk including the URL of the record and the reason for the withdrawal request.



eprints@whiterose.ac.uk
<https://eprints.whiterose.ac.uk/>

1 **Magnetic properties of gas hydrate-bearing sediments and their**
2 **association with iron geochemistry in the Sea of Marmara, Turkey**

3
4 Hailin Yang ^{a,b,*}, Peng Zhang ^c, Hailong Lu ^{a,*}, Meinan Shi ^d, Jianming Li ^e, Yinghan
5 Lu ^a, Yujia Liu ^a, Livio Ruffine ^f, Simon W. Poulton ^b
6

7 ^a Beijing International Center for Gas Hydrate, School of Earth and Space Sciences, Peking
8 University, Beijing 100871, China

9 ^b School of Earth and Environment, University of Leeds, Leeds LS2 9JT, UK

10 ^c State Key Laboratory of Loess and Quaternary Geology, Institute of Earth Environment, Chinese
11 Academy of Sciences, Xi'an 710061, China

12 ^d School of Ocean Sciences, China University of Geoscience, Beijing 100083, China

13 ^e Research Institute of Petroleum Exploration and Development, PetroChina, Beijing 100083, China

14 ^f Ifremer, Univ Brest, CNRS, UMR Geo-Ocean, F-29280 Plouzané, France

15
16 * Corresponding author *E-mail address*: hlu@pku.edu.cn (H. Lu), hyang@pku.edu.cn (H. Yang).

17 **Abstract**

18 The anaerobic oxidation of methane, a key geochemical process that is involved in the cycling
19 of sulfate and iron (oxyhydr)oxides in marine sediments, results in the formation of iron sulfides.
20 Although ferrimagnetic iron sulfides have been identified in seepage systems, the link between iron
21 migration and sediment magnetic properties remains poorly understood. Here, we investigate two
22 cores from the Sea of Marmara to evaluate biogeochemical iron cycling and iron sulfide mineralogy
23 in gas hydrate-bearing sediments. Magnetic analyses indicate the presence of greigite and pyrrhotite
24 in a core from a hydrate-rich site with a high hydrocarbon flux, which contrasts with a lack of these
25 minerals in a core characterized by only mild seepage. This is supported by the results of rock
26 magnetic and scanning electron microscope analyses of the sediments. The presence of authigenic
27 greigite is critical for assessing local redox records and together with the occurrence of monoclinic
28 pyrrhotite may suggest specific diagenetic processes in gas hydrate environments. Our analysis
29 demonstrates the usefulness of these ferrimagnetic minerals, with a high saturation isothermal
30 remanent magnetization to magnetic susceptibility ratio ($SIRM/\chi > 15 \text{ kAm}^{-1}$) and a high index of
31 hysteresis parameters ($D_{JH} > 0.2$) indicative of magnetic mineralogy changes, for evaluating
32 variability in the intensity of seepage fluxes and for estimating gas hydrate distributions.

33

34 **Keywords**

35 Iron geochemistry
36 Magnetic properties
37 Sea of Marmara
38 Seepage activity
39 Gas hydrate
40 Sediments

41 **1. Introduction**

42 The nature of iron sulfide minerals formed during diagenesis (*e.g.*, pyrite (FeS_2), greigite
43 (Fe_3S_4), pyrrhotite (Fe_{1-x}S)) in gas hydrate-bearing systems commonly exerts a significant influence
44 on the magnetic properties of associated marine sediment (Bertolin et al., 1995; Roberts and Weaver,
45 2005; Horng and Roberts, 2006; Merinero et al., 2008; Roberts, 2015; Kars and Kodama, 2015;
46 Zheng et al., 2016). In such sediments, the rate of anaerobic oxidation of methane (AOM) tends to
47 correlate positively with the upward migrating methane flux (Borowski et al., 2013), with sulfate
48 reduction coupled to AOM (sulfate-AOM) producing hydrogen sulfide that reacts with Fe^{2+} to form
49 the iron sulfide minerals (Jørgensen, 1990; Mazumdar et al., 2012; Horng, 2018). In these reactions,
50 dissolved ferrous iron is a key reactant and its availability is controlled by local redox conditions
51 (Lim et al., 2011; Lin et al., 2016). Compared with sulfate, Fe (oxyhydr)oxides are more energetically
52 favorable electron acceptors during AOM, particularly below the sulfate-methane transition zone
53 (SMTZ) in deep-sea sediments (Yang et al., 2021). However, the specific geochemical pathway
54 involving iron during AOM (Fe-AOM) is unresolved, and the origin of the dissolved iron remains
55 unclear (Boetius et al., 2000; Gorlas et al., 2018; Luo et al., 2020).

56 High pyrite concentrations may occur in the SMTZ, and its preservation in the geological record
57 has been suggested as a possible proxy for sustained methane delivery from deeper sediments (Chen
58 et al., 2006; Lim et al., 2011; Lin et al., 2016). While magnetic minerals, such as iron sulfides and
59 (oxyhydr)oxides, also occur in methane-rich sediments associated with gas hydrates, the nature of
60 this association has not been adequately resolved (Musgrave et al., 2006; Larrasoña et al., 2007; Lin
61 et al., 2021). The magnetic properties and paleomagnetic signature of host sediments are altered by
62 the characteristics of the iron minerals that form as a result of *in-situ* increases in methane or gas
63 hydrate. Complex interplays of factors, including the availability of dissolved iron, sedimentation
64 rate, and fluid and gas circulation, determine the dissolution and precipitation of iron minerals (Yang
65 et al., 2018; Chen et al., 2021). However, changes in sediment magnetic properties during generation
66 of authigenic iron sulfides from other iron minerals have not been fully explored in either
67 experimental or field studies.

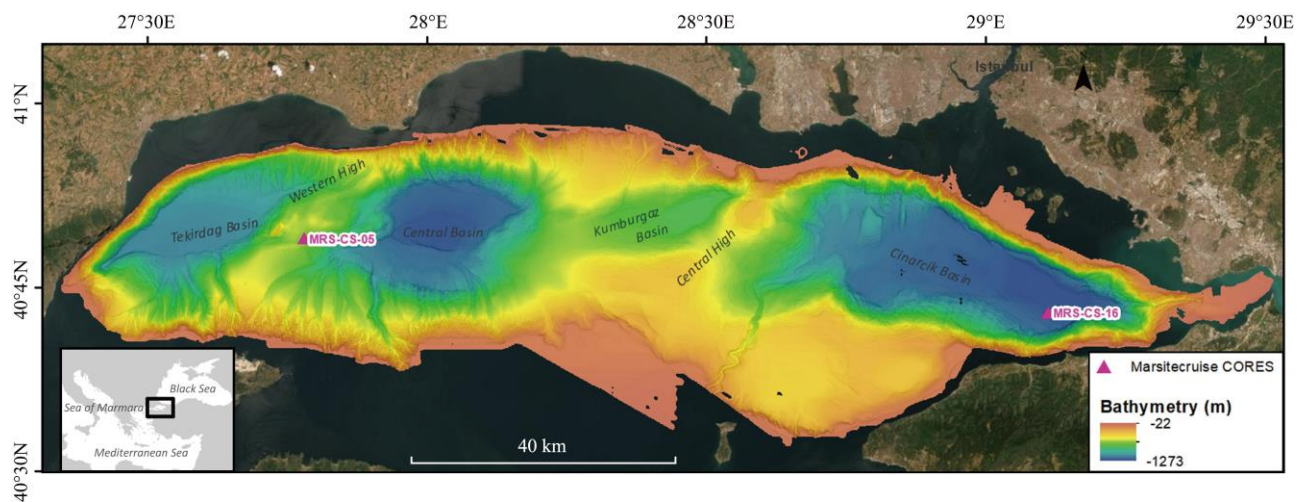
68 Here, we report magnetic properties for two sediment cores from the Sea of Marmara (SoM),
69 Turkey, combined with high-definition scanning electron microscope observations of iron sulfide
70 minerals and selective geochemical extractions of Fe phases. Our aim is to identify whether
71 ferrimagnetic iron sulfides such as greigite and pyrrhotite are present, and if so, to clarify their

72 formation and preservation pathways, as well as their potential as indicators of a high methane flux
73 related to the occurrence of gas hydrates.

74

75 2. Geological Background and Samples

76 The SoM is a semi-closed sea connecting the Black Sea to the Mediterranean Sea (Fig. 1). It
77 is located in an area characterized by high seismic activity owing to the presence of the North
78 Anatolian Fault, which facilitates upward fluid migration to the sea floor, and seawater infiltration
79 into the sediment (Ambraseys, 2002; Dupré et al., 2012; Géli et al., 2018; Grall et al., 2018; Henry
80 et al., 2018). The SoM has three main basins – the Tekirdağ and Çınarcık basins in the west and east,
81 respectively, and the Central basin (Okay et al., 2000; Şengör et al., 1985; Sorlien et al., 2012;
82 Çağatay and Uçarkuş, 2019). These basins are separated by two highs – the Western High and the
83 Central High (Fig. 1). Gas emissions are widespread in the SoM, and result from mixing of gases
84 originating from thermogenic, microbial or mantle sources (Géli et al., 2008; Bourry et al., 2009;
85 Burnard et al., 2012; Ruffine et al., 2018a; Ruffine et al., 2018b).



86

87 **Fig. 1.** Location map of the Western High (core MRS-CS-05, where gas hydrates have been discovered) and
88 Çınarcık Basin (core MRS-CS-16, without gas hydrate) in the Sea of Marmara.

89

90 Samples were collected during the MarsiteCruise expedition in November 2014 onboard the
91 R/V *Pourquoi Pas?*. Two 10-m-long cores were collected with a piston corer (Calypso®) from the
92 Western High (core MRS-CS-05) and the Çınarcık Basin (core MRS-CS-16) (Fig. 1). After recovery,
93 the cores were cut and sampled in the ship-based laboratory. Subsamples at 1 m intervals were
94 vacuum freeze-dried for subsequent analyses. Gas hydrates were recovered from the Western High,

95 where hydrate-bound gases are primarily of thermogenic origin, comprising CH₄ (82–87%), heavy
96 hydrocarbons (4.6–8.9%), and relatively high CO₂ concentrations (7.6–8.6%). By contrast, gas
97 hydrate is not present in the Çınarcık Basin, and instead primary microbial gases occur, comprising
98 a high CH₄ concentration (> 99.6%) and trace amounts of heavy hydrocarbons (< 0.01%) and CO₂
99 (< 0.1%) (Ruffine et al., 2018c).

100 The sedimentary sequence in core MRS-CS-05 from the Western High consists of an upper
101 marine unit (~0–3.5 mbsf) and an underlying lacustrine unit, whereas the sequence in core MRS-CS-
102 16 from the Çınarcık Basin comprises only the upper marine unit. The marine unit of core MRS-CS-
103 05 is composed of dark green-gray silty clay with total organic matter (TOC) content of 1.7 ± 0.4
104 wt% and total iron sulfide content of 0.7 ± 0.2 wt%, and the lacustrine unit contains brecciated and
105 soupy structures, which can be attributed to gas hydrate dissociation. The marine unit of core MRS-
106 CS-16 is a hemipelagic greenish-gray mud sequence, with a TOC content of 1.2 ± 0.2 wt% and a
107 total iron sulfide content of 0.5 ± 0.2 wt%, and is interrupted by numerous sandy turbidites and gas
108 expansion voids (Yang et al., 2018; Liu et al., 2019).

109 The Holocene sedimentation rate is lower in the Western High (~0.2–0.5 m/ka) than in the
110 Çınarcık Basin (~1–2 m/ka; Çağatay et al., 2000; Çağatay et al., 2009; Çağatay et al., 2015). Thus,
111 the core from the Western High records environmental and geological changes through the Late-
112 Pleistocene to Holocene, including a warm/wet climatic period and marine transgression from the
113 Mediterranean at ~12.6 kyr (Major et al., 2002; Vidal, 2010; Eriş et al., 2012; Çağatay et al., 2015).
114 The core from the Çınarcık Basin captures more recent, hemipelagic sedimentation from ~7.7 kyr to
115 the present (Liu et al., 2021).

116

117 **3. Material and Methods**

118 **3.1. Magnetic measurements**

119 Sediment magnetic susceptibility (χ) was measured using a Bartington Instruments MS2
120 magnetic susceptibility meter. Temperature dependence of low-field magnetic susceptibility (χ -T)
121 was measured in an argon atmosphere using an AGICO MFK1-FA Kappabridge magnetic
122 susceptibility meter. Hysteresis loop and isothermal remanent magnetization (IRM) measurements,
123 limited to a maximum field of 1T, were performed with a MicroMag 3900 alternating-gradient
124 magnetometer. The IRM imparted with a 1T field is referred to as saturation IRM (SIRM). First-
125 order reversal curves (FORCs) were measured (Pike et al., 1999) and FORC diagrams were processed

126 with the FORCinel software (Harrison and Feinberg, 2008). Low-temperature magnetic
127 measurements were also conducted using a Quantum Design Magnetic Properties Measurement
128 System (MPMS). Housen and Musgrave (1996b) proposed an index D_{JH} , which is the ratio of the
129 hysteresis parameters $(M_{rs}/M_s)/(B_{cr}/B_c)$, to identify magnetic mineralogy changes associated with gas
130 hydrates. M_{rs} is the saturation remanence, M_s is the saturation magnetization, B_{cr} is the remanent
131 coercive field, and B_c is the coercive field.

132

133 **3.2. Iron speciation and mineral analysis**

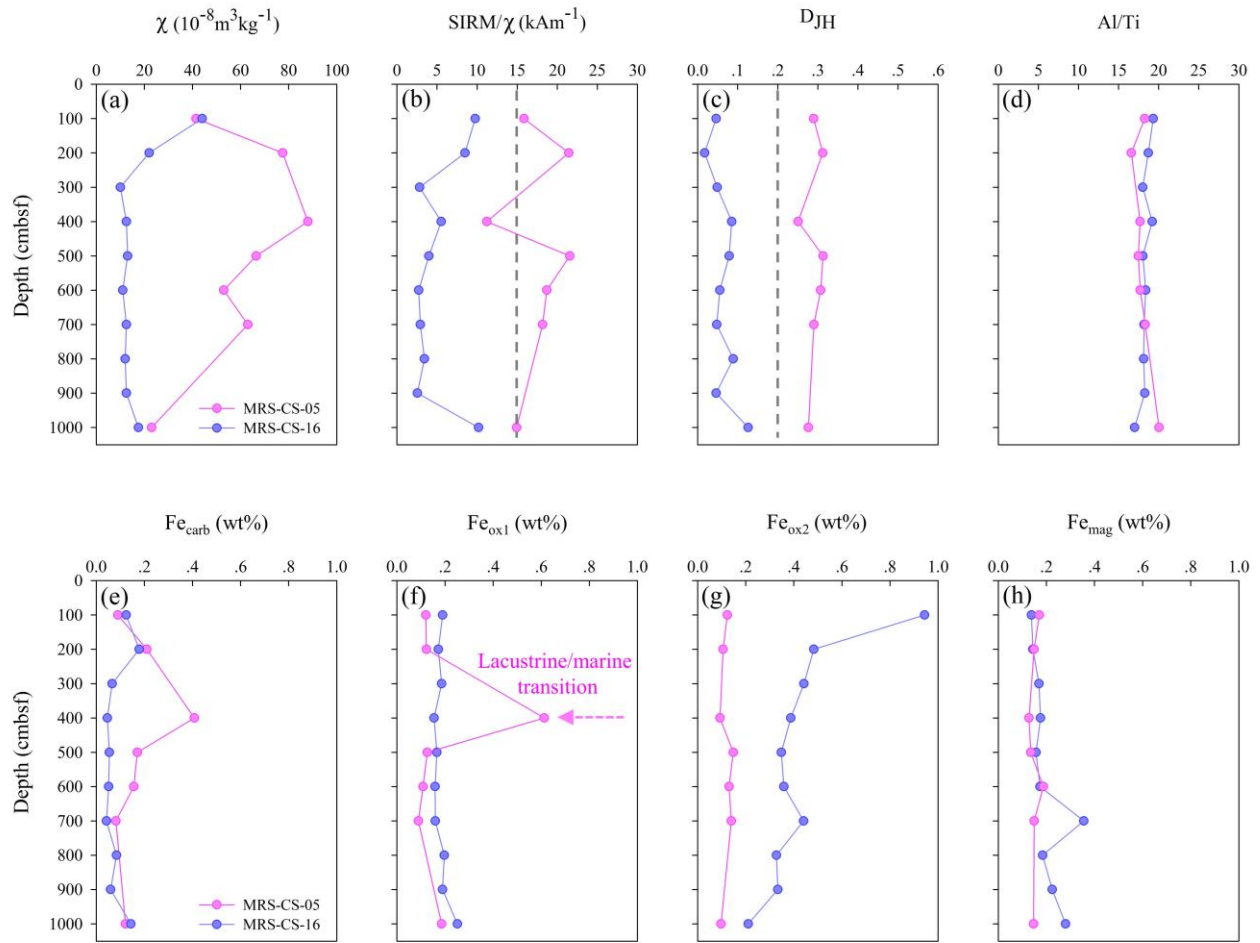
134 The sequential extraction procedure of Poulton and Canfield (2005) was used to determine
135 operationally-defined Fe pools. Target phases include Fe carbonates (*e.g.*, siderite and ankerite)
136 extracted with sodium acetate for 24 h (Fe_{carb}); easily reducible Fe (oxyhydr)oxides (*e.g.*, ferrihydrite
137 and lepidocrocite) extracted with hydroxylamine–hydrochloride for 48 h (Fe_{ox1}); reducible,
138 crystalline iron (oxyhydr)oxides (*e.g.*, goethite, akageneite and hematite) extracted with sodium
139 dithionite for 2 h (Fe_{ox2}), and mixed ferrous-ferric minerals (*e.g.*, magnetite) extracted with
140 ammonium oxalate for 6 h (Fe_{mag}). Fe contents in each extraction solution were determined using
141 inductively coupled plasma optical emission spectrometry (ICP-OES). Bulk Al and Ti contents were
142 determined by ICP-OES after microwave digestion. The concentrations of these elements were within
143 the certified ranges, with precision better than 3%. To provide more detailed information about the
144 main Fe phases extracted in each step, a subsample was investigated by X-ray powder diffraction
145 (PANalytical X'Pert Pro). An additional subsample was used to determine iron sulfide mineral
146 morphology, which was determined using a focused ion beam-scanning electron microscope (FIB-
147 SEM, Helios NanoLab 650) equipped with an energy dispersive X-ray spectrometry (EDS).

148

149 **4. Results**

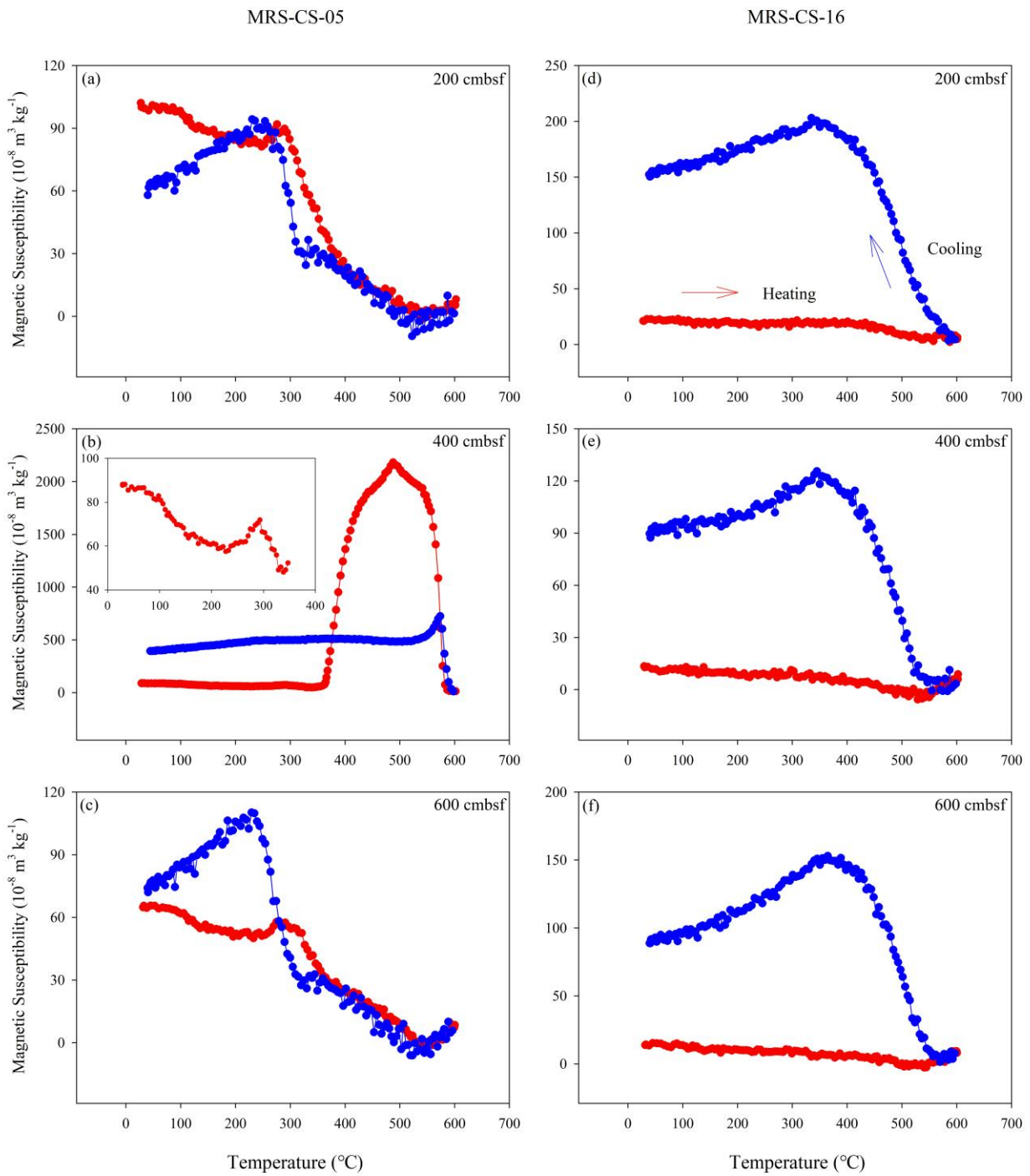
150 **4.1. Magnetic properties**

151 Low χ values (almost $< 20 \times 10^{-8} \text{ m}^3/\text{kg}$) were measured in core MRS-CS-16; while χ for samples
152 from core MRS-CS-05 has higher values (mainly $> 40 \times 10^{-8} \text{ m}^3/\text{kg}$), with a maximum value at 400
153 cmbsf depth (Fig. 2a). SIRM/ χ values are generally higher in core MRS-CS-05 relative to core MRS-
154 CS-16 (Fig. 2b). The magnetic index D_{JH} is also higher in samples from core MRS-CS-05
155 (0.25–0.31) than those in core MRS-CS-16 (average 0.06) (Fig. 2c).



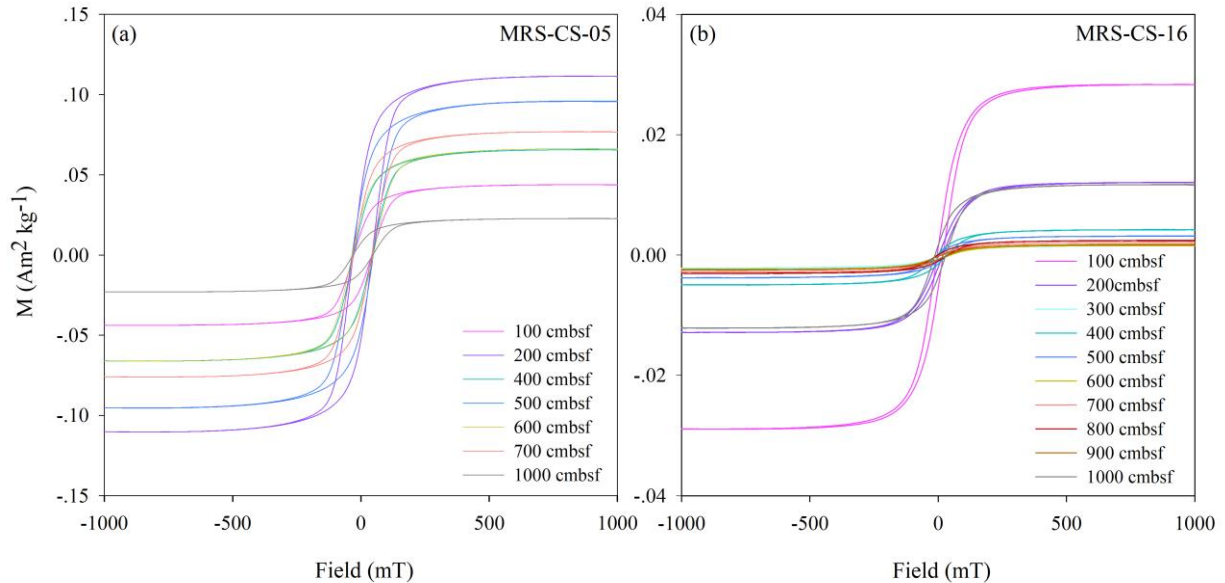
156
 157 **Fig. 2.** Downcore magnetic parameter and geochemical trends. **(a)** Magnetic susceptibility (χ), **(b)** SIRM/ χ , **(c)** D_{JH}
 158 (M_{rs}/M_s versus B_{cr}/B_c), **(d)** Al/Ti ratio, and **(e–h)** operationally-defined Fe phases determined via sequential
 159 extraction. The dominant mineral phases in each Fe pool are: Fe_{carb} : siderite; Fe_{ox1} : lepidocrocite; Fe_{ox2} : hematite;
 160 and Fe_{mag} : magnetite. Dashed lines in (b) and (c) refer to threshold parameters for identifying ferrimagnetic iron
 161 sulfide and gas hydrate occurrences.

162
 163 χ -T curves (Fig. 3) have different behavior for the two cores. In core MRS-CS-05, the curves
 164 for samples from 200 and 600 cmbsf are similar (Fig. 3a, c). Notably, for a sample from 400 cmbsf,
 165 the heating curve rises sharply at $\sim 370^\circ\text{C}$ and then decreases and approaches zero at 580°C (Fig. 3b).
 166 By contrast, there is no notable difference among χ -T curves for samples from core MRS-CS-16 (Fig.
 167 3d–f).



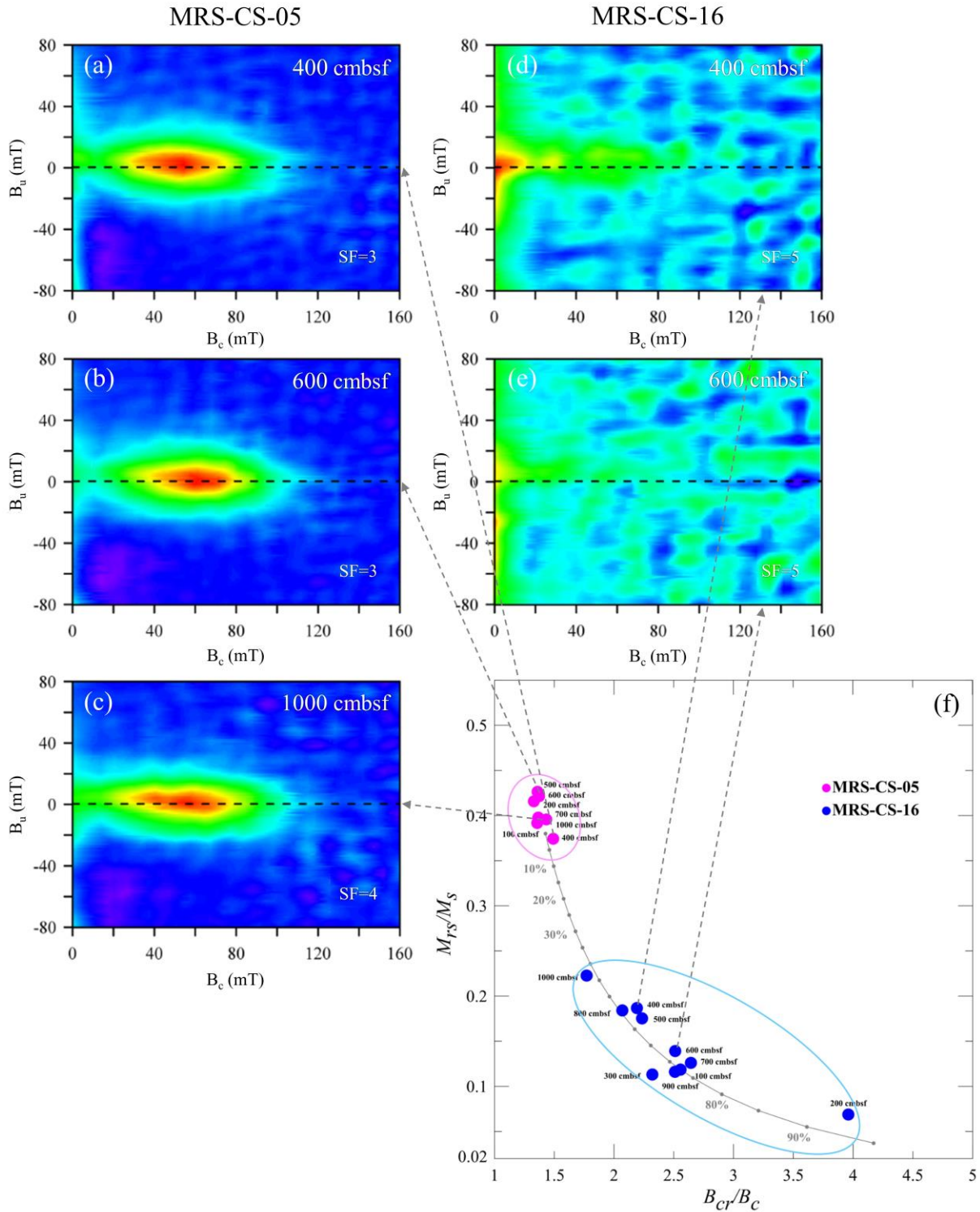
168
 169 **Fig. 3.** Magnetic susceptibility versus temperature (χ -T) curves for selected samples from cores MRS-CS-05 (a-c)
 170 and MRS-CS-16 (d-f). Red and blue lines denote heating and cooling curves, respectively.

172 Hysteresis loops for samples from two cores are shown in Fig. 4. Hysteresis loops for samples
173 from core MRS-CS-05 have relatively high coercivities and widths, with S-shaped loops (Fig. 4a),
174 while the coercive forces for samples from core MRS-CS-16 are lower, with narrower sigmoidal
175 shaped hysteresis loops (Fig. 4b).



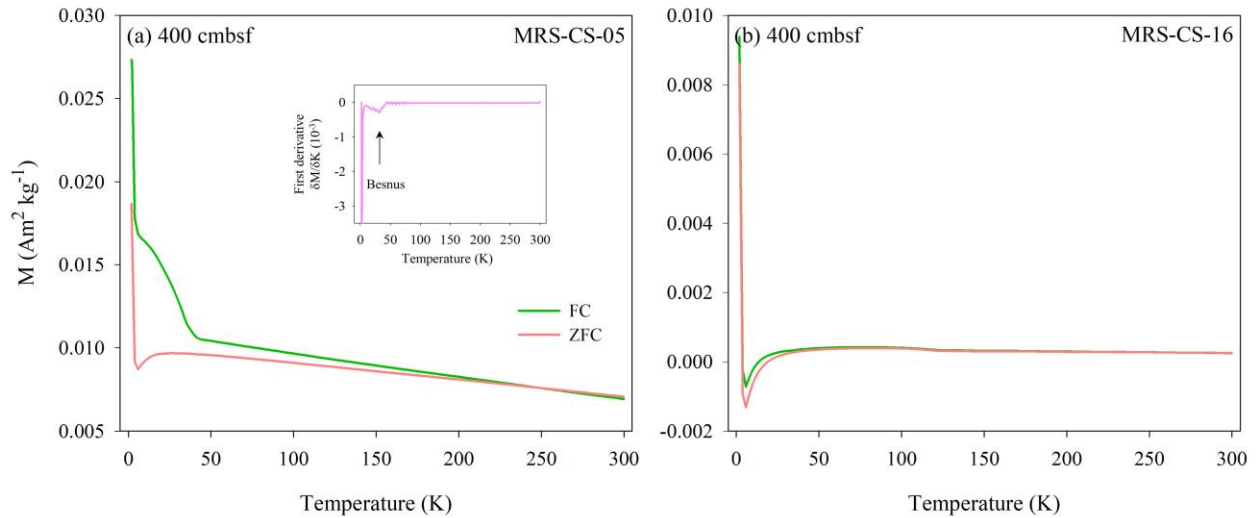
176
177 **Fig. 4.** Hysteresis loops for samples from the two cores from the Sea of Marmara. Results for (a) samples from
178 core MRS-CS-05, and (b) samples from core MRS-CS-16.

179
180 FORC diagrams further confirm the different magnetic properties of the two cores. The closed
181 oval-shaped contours with a central peak in FORC diagrams (Fig. 5a–c) and M_{rs}/M_s (Fig. 5f)
182 demonstrate that samples from MRS-CS-05 contain a high proportion of single domain (SD) greigite
183 (Roberts et al., 2006, 2011).



184
 185 **Fig. 5.** FORC diagrams and hysteresis ratios plotted on a Day plot (Day et al., 1977). (a), (b) and (c) Concentric
 186 contours and a large vertical spread are indicative of a significant SD contribution in core MRS-CS-05, which
 187 contrasts with the results from core MRS-CS-16 in (d), (e) and the blue oval zone in (f). B_u : interaction field among
 188 particles. SF: smoothing factor.

189
 190 Moreover, the Besnus transition at ~30–34K is recognizable in ZFC and FC curves for a sample
 191 from core MRS-CS-05 (Fig. 6a) due to the presence of monoclinic pyrrhotite (Besnus and Meyer,
 192 1964; Dekkers et al., 1989; Rochette et al., 1990; Horng and Roberts, 2018) and/or siderite (Housen
 193 et al., 1996a). However, there is no obvious Besnus transition in other samples from the two cores
 194 (Fig. 6b and Fig. S2).



195
 196 **Fig. 6** Zero field-cooled (ZFC) and field-cooled (FC) curves for representative samples from the two cores. Results
 197 indicate that (a) monoclinic pyrrhotite occurs at 400 cmbsf in core MRS-CS-05, and (b) neither a Besnus transition
 198 nor a Verwey transition are apparent in curves for a sample from core MRS-CS-16.

199
 200 **4.2 Sediment geochemistry**

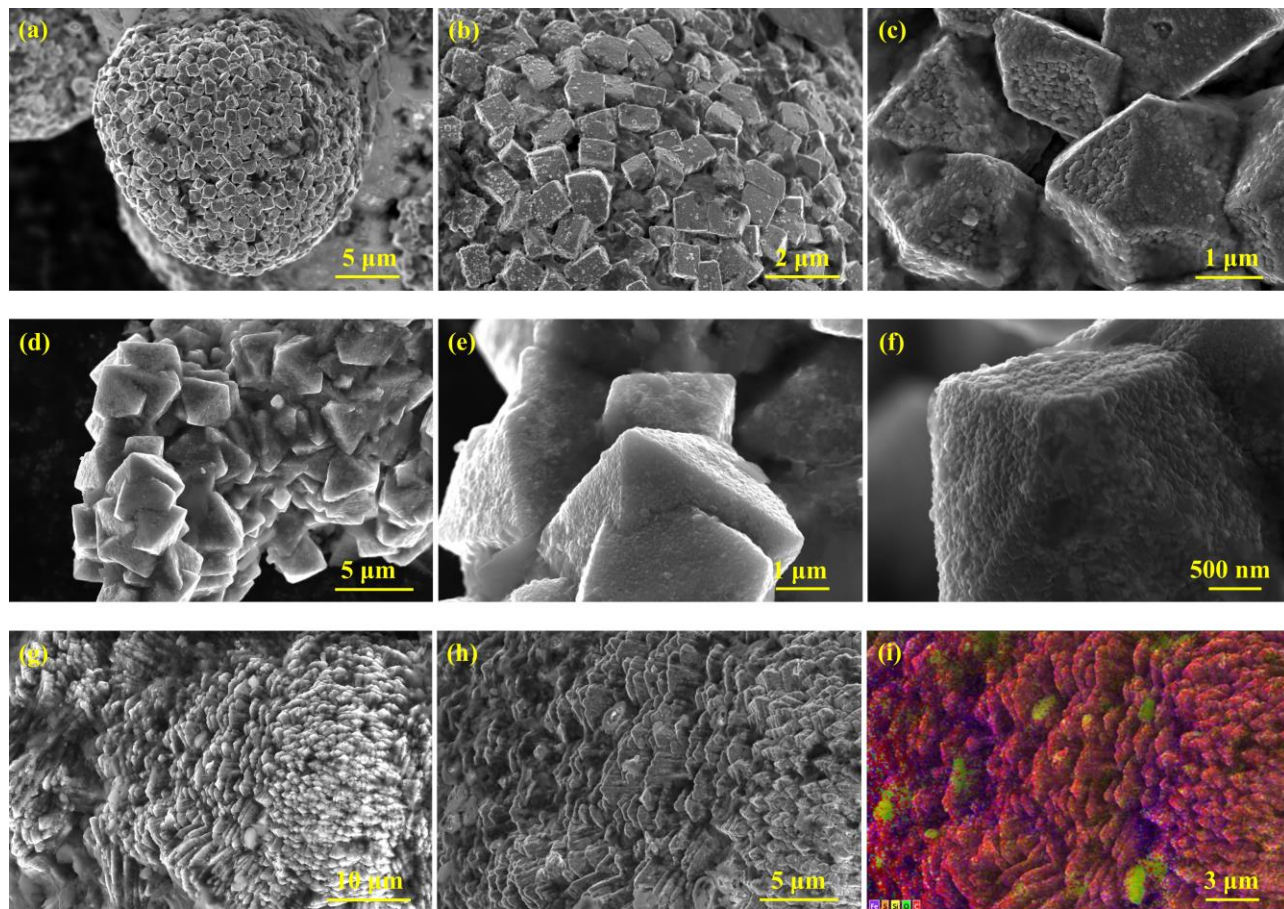
201 The Al/Ti ratio in the two cores is approximately 18.2 ± 0.2 wt% (Fig. 1d). Variations in Fe
 202 speciation are shown in Fig. 2e–h. Higher Fe_{carb} concentrations generally occur in samples from core
 203 MRS-CS-05 (ranging from 0.08 to 0.41 wt%) compared to those from core MRS-CS-16 (< 0.18 wt%)
 204 (Fig. 1e). Fe_{ox1} concentrations in both cores remain nearly constant at 0.19 ± 0.01 wt%, except for a
 205 sample from 400 cmbsf from core MRS-CS-05, where the concentration is 0.61 wt% (Fig. 1f). For
 206 Fe_{ox2} , the values in core MRS-CS-05 are relatively stable, with an average of 0.12 ± 0.02 wt%, while
 207 in core MRS-CS-16, Fe_{ox2} values are higher than 0.21 wt% and reach a peak of 0.94 wt% at 100
 208 cmbsf (Fig. 1g). The two cores have similar Fe_{mag} values (0.13–0.19 wt%) in the 100–600 cmbsf
 209 intervals, with a small increase at the bottom of core MRS-CS-16 (Fig. 1h). The SMTZ was

210 determined using porewater sulfate data from two additional cores taken close to the sampled cores
211 (Fig. S1) and the results indicate that the present-day SMTZ of the MRS-CS-05 site is close to the
212 sediment-water interface, which contrasts with the relatively deep SMTZ depth of ~200 cmbsf at the
213 MRS-CS-16 site. These SMTZ depths in the Çınarcık Basin and Western High are in agreement with
214 those of previous studies (Çağatay et al., 2004; Tryon et al., 2010).

215

216 4.3 FIB-SEM observations

217 Pyrite is observed by FIB-SEM at several depths in the two cores and can be used to indicate
218 methane activity. Framboidal pyrite represents the dominant pyrite morphology, but a variety of
219 morphologies occur, including isolated or clustered pyrite framboids, cubic and octahedral
220 microcrystals, and irregular pyrite aggregates (Fig. 7a–f).



221
222 **Fig. 7.** High-resolution images of pyrite and greigite (analysed by FIB-SEM) in samples from core MRS-CS-05.
223 (a)–(f) Different pyrite morphologies. Crystal edges in (c) and (f) may suggest nucleation processes affected by
224 methane seepage. (g) and (h) Fine-grained SD greigite. (i) EDS elemental mapping of greigite in (h).

225

226 **5. Discussion**

227 **5.1. Magnetic mineralogy of the sediment cores**

228 High χ values were observed previously in cores at ~400 cmbsf from the Western High, which
229 are considered to be associated with the lacustrine/marine transition and the sapropel layer (Drab et
230 al., 2015; Makaroğlu et al., 2020). Similar High SIRM/ χ values ($> 15 \text{ kAm}^{-1}$) in core MRS-CS-05
231 are potential indicators of ferrimagnetic greigite (Snowball and Thompson, 1988; Roberts, 1995;
232 Chen et al., 2021), which suggests that this mineral may be common in this core. For the sample from
233 400 cmbsf, the warming curve (Fig. 3b) has a decreasing trend between 300 and 400°C, which
234 probably reflects the occurrence of ferrimagnetic greigite and/or pyrrhotite (Maher and Thompson,
235 1999; Roberts et al., 2011). Another peak at ~480°C that subsequently decreases to zero at 580°C
236 indicates the Curie temperature of magnetite, which we attribute to the transformation of greigite to
237 magnetite at and above ~370°C during heating (Table S1; Dunlop and Özdemir, 1997). The Besnus
238 transition at 32K by the first derivative (Fig. 6a), approximate reversible heating and cooling curves
239 with a Curie temperature of ~320°C (Fig. 3b), and markedly high Mrs/Ms values and low Bcr/Bc
240 values all suggest that monoclinic 4C pyrrhotite is present, rather than its polytype hexagonal 3T
241 pyrrhotite or siderite (35–38K) (Dekkers, 1989; Frederichs et al., 2003; Roberts, 2015; Horng, 2018).
242 Magnetic property measurements, together with FIB-SEM-EDS imaging, provide evidence that SD-
243 sized greigite is the primary remanence carrier in core MRS-CS-05. These magnetic anomalies are
244 consistent with the finding that high D_{JH} values (> 0.2) are indicative of gas hydrates (Housen and
245 Musgrave 1996b; Kars and Kodama, 2015).

246

247 **5.2. Factors affecting magnetic characteristics**

248 Al and Ti, which are conservative elements during chemical weathering and diagenesis (Nesbitt
249 and Markovics, 1997; Wei et al., 2003), are commonly used to estimate the abundance of terrigenous
250 material in sedimentary environments (Murray and Leinen, 1996). The relatively consistent and
251 stable Al/Ti ratios suggest a similar detrital origin for the two cores. Hence, the variability in iron
252 speciation, as a redox sensitive proxy, dominantly reflects differences in local redox conditions and
253 Fe mineral transformations, rather than variability in the detrital mineral input. Authigenic greigite
254 and pyrrhotite in core MRS-CS-05 (Fig. 3a–c, Fig. 5a–c, Fig. 6a, Fig. 7g–i) are intermediate mineral
255 phases during the formation of pyrite (Gagnon et al., 1995; Roberts and Weaver, 2005). Framboidal

256 pyrite can form in syn- and early-diagenesis and its precise morphology may reflect specific
257 environmental and geochemical parameters (Wilkin et al., 1996; Çağatay et al., 2004; Chang et al.
258 2020). A peak in pyrite concentrations in methane seepage sediments commonly indicates the
259 location of the SMTZ (Larrasoña et al., 2007; Dewangan et al, 2013). However, because greigite is
260 also widespread throughout the core, the pyrite concentration profile considered in isolation, likely
261 does not indicate the present-day SMTZ position.

262 Previous studies suggest that under appropriate conditions, such as during rapid sedimentation
263 with an associated upward SMTZ shift, preservation of greigite rather than pyrite may dominate in
264 continental margin sediments (Greve et al., 2021). The sedimentation rate and SMTZ in the Western
265 High (MRS-CS-05) is lower than that in the Çınarcık Basin (MRS-CS-16) (Çağatay et al., 2004), so
266 magnetic mineral diagenesis in core MRS-CS-05 is more likely linked to a strong fluid flux due to
267 gas hydrate dissociation, with the SMTZ occurring close to the seafloor. Indeed, near seafloor gas
268 hydrate formation and decomposition were previously reported from the Western High by Tryon et
269 al. (2010) and Ruffine et al (2018b, c), which also plays a key role in pore-water salinity, which in
270 turn is likely to be an important controlling factor during greigite preservation (Chen et al., 2021).
271 However, the abrupt increase in Fe_{carb} and Fe_{ox1} minerals (Fig. 2e, f) and the decrease in greigite (Fig.
272 2b) below ~400 cmsf in core MRS-CS-05 are mainly due to the low-salinity and sulfate-limited
273 lacustrine conditions in the Sea of Marmara before ~12.6 ka.

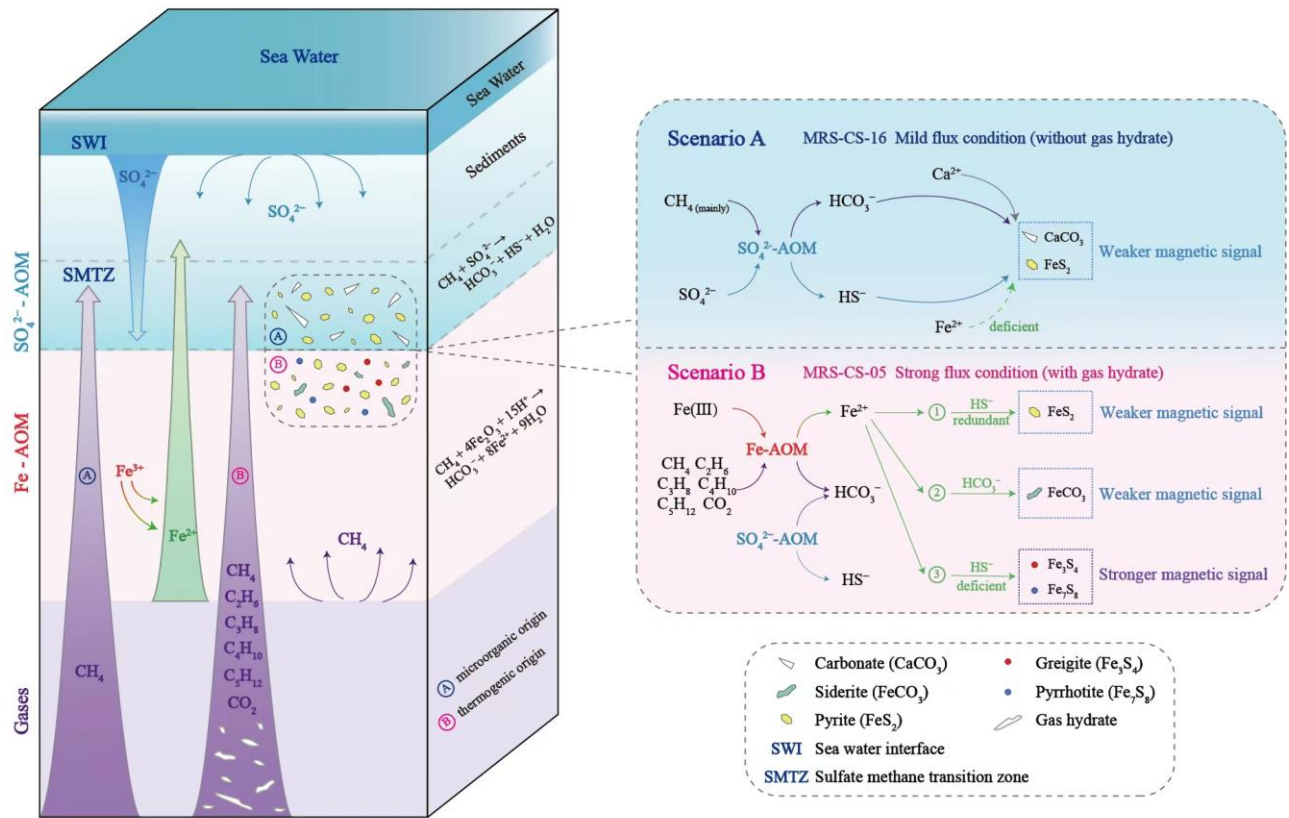
274

275 **5.3. Iron pools and pathways**

276 During Fe mineral diagenesis, the magnetic characteristics of core MRS-CS-05 changed
277 dramatically, due to the formation and preservation of authigenic greigite and pyrrhotite. Although
278 the two cores have similar Fe concentrations in the Fe_{mag} pool (with a possible slight relative increase
279 in the deeper sediments of core MRS-CS-16; Fig. 2h), magnetite may not contribute significantly to
280 the magnetic susceptibility because of the reducing sedimentary conditions, as discussed below. In
281 addition, the ferric-Fe pools (i.e., Fe_{ox1} and Fe_{ox2} , which dominantly comprise lepidocrocite and
282 hematite, respectively) generally have low and stable concentrations in core MRS-CS-05, with the
283 exception of the peak in Fe_{ox1} linked to the development of lacustrine conditions with sulfate
284 limitation (Fig. 2f). These low concentration ferric-Fe pools are accompanied by the presence of
285 reduced non-sulfidic Fe phases in the Fe_{carb} pool (*e.g.*, siderite; Fig. 2e), and Fe sulfides such as
286 greigite, pyrrhotite and pyrite (Fig. 3a–c, Fig. 5a–c, Fig. 6a, Fig.7g–i). We conclude that the primary

287 reactive iron (oxyhydr)oxides in MRS-CS-05 were subjected to strongly reducing and acidic
 288 conditions, which were associated with upward migrating hydrate-bound gases and methanogenesis,
 289 thus producing dissolved Fe(II), which subsequently formed iron sulfide minerals, thereby
 290 dramatically changing the sediment magnetic properties .

291 The above observations indicate that the occurrence and preservation of greigite and pyrrhotite
 292 in marine sediments has important implications for the interpretation of magnetic records. Two
 293 scenarios can be considered to explain the magnetic properties and iron mineralogy in the two cores
 294 (Fig. 8). Scenario A involves methane production and consumption during early diagenesis, where
 295 sulfate-driven AOM results in the precipitation of pyrite and calcite (which is precipitated
 296 preferentially over siderite). This scenario may result in low Fe_{carb} concentrations (*e.g.*, Fig. 2e) and
 297 the weak magnetism observed for core MRS-CS-16. Here, detrital iron (oxyhydr)oxides (*e.g.*,
 298 hematite) may be the main contributor to the χ values (Table S2, $r = 0.872$).



299
 300 **Fig. 8.** Two scenarios involving different iron geochemical pathways that may explain the magnetic properties and
 301 mineralogy observed in the two cores. Scenario A is the most common in a methane seepage environment, with
 302 paramagnetic iron sulfides formed in sediments due to sulfate-AOM. Scenario B proposes Fe-AOM as a significant

303 factor associated with reductive dissolution of Fe (oxyhydr)oxides, which results in the precipitation of sulfide
304 minerals such as greigite and pyrrhotite, with a major change in the local magnetic characteristics.

305
306 In scenario B, post-depositional processes in gas hydrate sediments are affected by a strong
307 hydrocarbon flux. The associated fluids, with high CO₂ concentrations and heavy hydrocarbons, exert
308 a strong influence on redox conditions and pH, thereby enhancing the dissolution of detrital iron
309 (oxyhydr)oxides, as observed in core MRS-CS-05 (Fig. 2f, g). The dissolved Fe(II) results in different
310 potential geochemical pathways (1, 2 and 3 in Fig. 8). If HS⁻ and HCO₃⁻ from AOM are abundant,
311 pyrite and siderite are the dominant phases formed, with little change in magnetic properties
312 (pathways 1 and 2). However, when the SMTZ is located near the seafloor, HS⁻ is deficient in
313 porewaters, leading to greigite and pyrrhotite formation. This provides an explanation for the down-
314 core magnetic property evolution of core MRS-CS-05 (pathway 3). Under such conditions, Fe-driven
315 AOM (Fe^{III} oxides + CH₄ + H⁺ → Fe^{II} + HCO₃⁻ + H₂O) likely exerts a strong influence on the
316 magnetic minerals formed.

317

318 **6. Conclusions**

319 Magnetic property measurements and geochemical data, combined with electron microprobe
320 imaging, were systematically conducted on two cores from the Sea of Marmara. The presence of
321 authigenic greigite and monoclinic pyrrhotite are inferred in the core from the Western High, which
322 was sampled in a current seepage with abundant gas hydrate distribution. This authigenic mineral
323 suite was formed due to upward-migrating fluids that contain dissolved methane and high
324 concentrations of CO₂ and heavy hydrocarbons. Our findings establish a close relationship between
325 sediment magnetic properties, diagenetic iron cycling, and the presence of gas hydrate. Based on the
326 observed magnetic property changes, specific geochemical iron cycling pathways may explain
327 greigite and pyrrhotite formation. It appears that salinity and hydrogen sulfide are also factors that
328 favor preservation of these iron sulfides. Therefore, rock magnetism combined with geochemical data
329 are promising tools for constraining gas hydrate distributions in both modern and ancient settings.

330

331 **Declaration of Interests**

332 The authors declare that they have no known competing financial interests or personal
333 relationships that could have appeared to influence the work reported in this paper.

334

335 **Acknowledgments**

336 We thank Hailiang Dong for editorial assistance, and Andrew P. Roberts, M. Namık Çağatay
337 and two other anonymous reviewers for constructive comments that significantly improved the
338 manuscript. This work was supported by the China Geological Survey Project (DD20189310,
339 DD20190230, DD20221703), the Guangdong Major Project of Basic and Applied Basic Research
340 (2020B0301030003), the Fundamental Research Funds for the Central Universities (2652017129),
341 and China Scholarship Council (202006015014). We greatly appreciate the captain, crew, and help
342 with sampling from the onboard scientists of the *Pourquoi Pas?*.

343

344 **Data Availability**

345 Data are available in a public archive at <https://data.mendeley.com/datasets/g49fnbcm78/3>

346

347 **References**

- 348 Ambraseys, N., 2002. The seismic activity of the Marmara Sea region over the last 2000 years. Bull. Seismol.
349 Soc. Am. 92, 1–18. <http://dx.doi.org/10.1785/0120000843>
- 350 Bertolin, A., Frizzo, P., Rampazzo, G., 1995. Sulphide speciation in surface sediments of the Lagoon of Venice:
351 A geochemical and mineralogical study. Mar. Geol. 123, 73–86. [https://doi.org/10.1016/0025-](https://doi.org/10.1016/0025-3227(95)80005-V)
352 [3227\(95\)80005-V](https://doi.org/10.1016/0025-3227(95)80005-V)
- 353 Besnus, M.J., Meyer, A.J. 1964. Nouvelles données expérimentales sur le magnétisme de la pyrrhotine naturelle.
354 Paper presented at Proceedings of the International Conference on Magnetism, Nottingham, England, pp.
355 507–511.
- 356 Boetius, A., Ravensschlag, K., Schubert, C.J., 2000. A marine microbial consortium apparently mediating
357 anaerobic oxidation of methane. Nature 407, 623–626. <https://doi.org/10.1038/35036572>
- 358 Borowski, W.S., Rodriguez, N.M., Paull, C.K., Ussler III, W., 2013. Are ³⁴S-enriched authigenic sulfide minerals
359 a proxy for elevated methane flux and gas hydrates in the geologic record? Mar. Petrol. Geol. 43, 381–395.
360 <https://doi.org/10.1016/j.marpetgeo.2012.12.009>
- 361 Bourry, C., Chazallon, B., Charlou, J-L, Donval, J.P, Ruffine, L., Henry, P., Geli, L., Çağatay, M.N., İnan, S.,
362 Moreau, M., 2009. Free gas and gas hydrates from the Sea of Marmara, Turkey: Chemical and structural
363 characterization. Chem. Geol. 264, 197–206. <https://doi.org/10.1016/j.chemgeo.2009.03.007>
- 364 Burnard, P., Bourlange, S., Henry, P., Geli L. Tryon, M.D., Natal'in, B., Sengör, A.M.C., Özeren M.S., Çağatay
365 M.N., 2012. Constraints on fluid origins and migration velocities along the Marmara Main Fault (Sea of

366 Marmara, Turkey) using helium isotopes. *Earth Planet. Sci. Lett.* 341–344: 68–78.
367 <https://doi.org/10.1016/j.epsl.2012.05.042>

368 Çağatay, M.N., Erics, K., Ryan, W.B.F., Sancar, Ü., Polonia, A., Akçer, S., Biltekin, D., Gasperini, L., Görür, N.,
369 Lericolais, G., Bard, E., 2009. Late Pleistocene–Holocene evolution of the northern shelf of the Sea of
370 Marmara. *Mar. Geol.* 265, 87–100. <https://doi.org/10.1016/j.margeo.2009.06.011>

371 Çağatay, M.N., Görür, N., Algan, O., Eastoe, C., Tchapylyga, A., Ongan, D., Kuhn, T., Kuşcu, I., 2000. Late
372 Glacial–Holocene palaeoceanography of the Sea of Marmara: Timing of connections with the Mediterranean
373 and the Black Seas. *Mar. Geol.* 167, 191–206. [https://doi.org/10.1016/S0025-3227\(00\)00031-1](https://doi.org/10.1016/S0025-3227(00)00031-1)

374 Çağatay, M.N., Özcan, M., Güngör, E. 2004. Pore-water and sediment geochemistry in the Marmara Sea
375 (Turkey): Early diagenesis and diffusive fluxes. *Geochem. Explor. Env. A.* 4, 213–225.
376 <https://doi.org/10.1144/1467-7873/04-202>

377 Çağatay, M.N., Uçarkuş, G., 2019. Morphotectonics of the Sea of Marmara: Basins and Highs on the North
378 Anatolian Continental Transform Plate Boundary. In: Duarte, J. (Ed.). *Transform Plate Boundaries and*
379 *Fracture Zones*, Elsevier, pp. 397–416. <https://doi.org/10.1016/B978-0-12-812064-4.00016-5>

380 Çağatay, M.N., Wulf, S. Guichard, F. Özmaral, A., Henry, P., Gasperini, L., 2015. The tephra record from the Sea
381 of Marmara for the last ca. 70 ka and its palaeoceanographic implications. *Mar. Geol.* 361: 96–110.
382 <https://doi.org/10.1016/j.margeo.2015.01.005>

383 Chang, J., Li, Y., Lu, H., 2022. The Morphological characteristics of authigenic pyrite formed in marine
384 sediments. *J. Mar. Sci. Eng.*, 10, 1533. <https://doi.org/10.3390/jmse10101533>

385 Chen, D.F., Feng, D., Su, Z., Song, Z.G., Chen, G.Q., Cathles III, L.M., 2006. Pyrite crystallization in seep
386 carbonates at gas vent and hydrate site. *Mater. Sci. Eng. C* 26, 602–605.
387 <https://doi.org/10.1016/j.msec.2005.08.037>

388 Chen, Y., Zhang, W., Nian, X., Sun, Q., Ge, C., Hutchinson, S.M., Cheng, Q., Wang, F., Chen, J., Zhao, X., 2021.
389 Greigite as an indicator for salinity and sedimentation rate change: Evidence from the Yangtze River Delta,
390 China. *J. Geophys. Res. Sol. Ea.* 126, e2020JB021085. <https://doi.org/10.1029/2020JB021085>

391 Day, R., Fuller, M., Schmidt, V. A., 1977. Hysteresis properties of titanomagnetites: Grain-size and
392 compositional dependence. *Phys. Earth Planet. Inter.* 13, 260–267. [https://doi.org/10.1016/0031-9201\(77\)90108-X](https://doi.org/10.1016/0031-9201(77)90108-X)

393

394 Dekkers M.J., Mattéi, J.L., Fillion, G., Rochette, P. 1989. Grain-size dependence of the magnetic behavior of
395 pyrrhotite during its low temperature transition at 34 K. *Geophys. Res. Lett.* 16,
396 855–858. <https://doi.org/10.1029/GL016i008p00855>

397 Dewangan, P., Basavaiah, N., Badesab, F.K., Usapkar, A., Mazumdar, A., Joshi, R., Ramprasad, T., 2013.
398 Diagenesis of magnetic minerals in a gas hydrate/cold seep environment off the Krishna–Godavari basin, Bay
399 of Bengal. *Mar. Geol.* 340, 57–70. <https://doi.org/10.1016/j.margeo.2013.04.016>

400 Drab, L., Carlut, J., Hubert-Ferrari, A., Martinez, P., LePoint, G., El Ouahabi, M., 2015. Palaeomagnetic and
401 geochemical record from cores from the Sea of Marmara, Turkey: Age constraints and implications of
402 sapropelic deposition on early diagenesis. *Mar. Geol.*, 360, 40–54.
403 <https://doi.org/10.1016/j.margeo.2014.12.002>

404 Dunlop D.J., Özdemir, Ö., 1997. *Rock magnetism: Fundamentals and frontiers*. Cambridge University Press, New
405 York.

406 Dupré, S., Scalabrin, C., Géli, L., Henry, P., Grall, C., Çağatay, N., Imren, C., the MARMESONET Scientific
407 Party Team., 2012. Widespread gas emissions in the Sea of Marmara, results from systematic ship-borne
408 multibeam echosounder water column imageries. 11th International Conference of Gas in Marine Sediments,
409 Nice.

410 Eriş, K.K., Çağatay, N., Beck, C., Lepinay, B.M.D., Corina, C., 2012. Late-Pleistocene to Holocene sedimentary
411 fills of the Çınarcık basin of the Sea of Marmara. *Sediment. Geol.* 281, 151–165.
412 <https://doi.org/10.1016/j.sedgeo.2012.09.001>

413 Frederichs, T., von Dobeneck, T., Bleil, U., Dekkers, M., 2003. Towards the identification of siderite,
414 rhodochrosite, and vivianite in sediments by their low-temperature magnetic properties. *Phys. Chem. Earth*
415 28, 669–679. [https://doi.org/10.1016/S1474-7065\(03\)00121-9](https://doi.org/10.1016/S1474-7065(03)00121-9)

416 Gagnon, C., Mucci, A., Pelletier, É., 1995. Anomalous accumulation of acid-volatile sulphides (AVS) in a coastal
417 marine sediment, Saguenay Fjord, Canada. *Geochimi. Cosmochimi. Acta* 59, 2663–2675.
418 [https://doi.org/10.1016/0016-7037\(95\)00163-T](https://doi.org/10.1016/0016-7037(95)00163-T)

419 Géli, L., Henry, P., Grall, C., Tary, J.-B., Lomax, A., Batsi, E., Riboulot, V., Cros, E., Gürbüz, C., Işık, S., 2018.
420 Gas and seismicity within the Istanbul seismic gap. *Sci. Rep.* 8, 6819. [https://doi.org/10.1038/s41598-018-](https://doi.org/10.1038/s41598-018-23536-7)
421 [23536-7](https://doi.org/10.1038/s41598-018-23536-7)

422 Géli, L., Henry, P., Zitter, T., Dupré, S., Tryon, M., Çağatay, M., de Lépinay, B., Le Pichon, X., engör, A., Görür,
423 N., 2008. Gas emissions and active tectonics within the submerged section of the North Anatolian Fault zone
424 in the Sea of Marmara. *Earth Planet. Sci. Lett.* 274, 34–39. <https://doi.org/10.1016/j.epsl.2008.06.047>

425 Gorlas, A., Jacquemot, P., Guigner, J-M., Gill, S., Forterre, P., Guyot, F., 2018. Greigite nanocrystals produced
426 by hyperthermophilic archaea of *Thermococcales* order. *PLoS One* 13, e0201549.
427 <https://doi.org/10.1371/journal.pone.0201549>

428 Grall, C., Henry, P., Dupré, S., Géli, L., Scalabrin, C., Zitter, T.A.C., Sengor, A.M.C., Çağatay, M.N., Cifci, G.,
429 2018. Upward migration of gas in an active tectonic basin: An example from the Sea of Marmara. *Deep-Sea*
430 *Res. Pt II* 153, 17–35. <https://doi.org/10.1016/j.dsr2.2018.06.007>

431 Greve, A., Kars, M., Dekkers, M.J., 2021. Fluid accumulation, migration and anaerobic oxidation of methane
432 along a major splay fault at the Hikurangi subduction margin (New Zealand): A magnetic approach. *J.*
433 *Geophys. Res. Sol. Ea.* 126, e2020JB020671. <https://doi.org/10.1029/2020JB020671>

434 Harrison, R.J., Feinberg, J.M., 2008. FORC_{in}el: An improved algorithm for calculating first-order reversal curve
435 distributions using locally weighted regression smoothing. *Geochem. Geophys. Geosy.* 9. <https://doi.org/10.1029/2008gc001987>

437 Henry, P., Grall, C., Kende, J., Viseur, S., Özeren, M.S., Şengör, A.M.C., Dupré, S., Saclabrin, C., Géli, L., 2018.
438 A statistical approach to relationships between fluid emissions and faults: The Sea of Marmara case. *Deep-Sea*
439 *Res. Pt II* 153, 131–143. <https://doi.org/10.1016/j.dsr2.2018.05.010>

440 Horng, C.-S., 2018. Unusual magnetic properties of sedimentary pyrrhotite in methane seepage sediments:
441 Comparison with metamorphic pyrrhotite and sedimentary greigite. *J. Geophys. Res. Sol. Ea.* 123,
442 4601–4617. <https://doi.org/10.1002/2017JB015262>

443 Horng, C.-S., Roberts, A.P., 2006. Authigenic or detrital origin of pyrrhotite in sediments?: Resolving a
444 paleomagnetic conundrum. *Earth Planet. Sci. Lett.* 241, 750–762. <https://doi.org/10.1016/j.epsl.2005.11.008>

445 Horng, C.-S., Roberts, A.P., 2018. The low-temperature Besnus magnetic transition: Signals due to monoclinic
446 and hexagonal pyrrhotite. *Geochem. Geophys. Geosystem.* 19, 3364–3375.
447 <https://doi.org/10.1029/2017GC007394>

448 Housen, B.A., Banerjee, S.K., Moskowitz, B. M., 1996a. Low temperature magnetic properties of siderite and
449 magnetite in marine sediments. *Geophys. Res. Lett.* 23, 2843–2846. <https://doi.org/10.1029/96GL01197>

450 Housen, B.A., Musgrave, R.J., 1996b. Rock-magnetic signature of gas hydrates in accretionary prism sediments.
451 *Earth Planet. Sci. Lett.* 139, 509–519. [https://doi.org/10.1016/0012-821X\(95\)00245-8](https://doi.org/10.1016/0012-821X(95)00245-8)

452 Jørgensen, B.B., 1990. A thiosulfate shunt in the sulfur cycle of marine sediments. *Science* 249, 152–154.
453 <https://doi.org/10.1126/science.249.4965.152>

454 Kars, M., Kodama, K., 2015. Authigenesis of magnetic minerals in gas hydrate-bearing sediments in the Nankai
455 Trough, offshore Japan. *Geochem. Geophys. Geosystem.* 16, 947–961.
456 <https://doi.org/10.1002/2014GC005614>

457 Larrasoaña, J. C., Roberts, A. P., Musgrave, R. J., Gràcia, E., Piñero, E., Vega, M., Martínez-Ruize F., 2007.
458 Diagenetic formation of greigite and pyrrhotite in gas hydrate marine sedimentary systems. *Earth Planet. Sci.*
459 *Lett.* 261, 350–366. <https://doi.org/10.1016/j.epsl.2007.06.032>

460 Lim, Y.C., Lin, S., Yang, T.F., Chen, Y-G., Liu, C.-S., 2011. Variations of methane induced pyrite formation in
461 the accretionary wedge sediments offshore southwestern Taiwan. *Mar. Petrol. Geol.* 28, 1829–1837.
462 <https://doi.org/10.1016/j.marpetgeo.2011.04.004>

463 Lin, Q., Wang, J., Algeo, T.J., Sun, F., Lin, R., 2016. Enhanced framboidal pyrite formation related to anaerobic
464 oxidation of methane in the sulfate-methane transition zone of the northern South China Sea. *Mar. Geol.* 379,
465 100–108. <https://doi.org/10.1016/j.margeo.2016.05.016>

466 Lin, Z., Sun, X. Roberts, A.P., Strauss, H. Lu, Y. Yang, X. Gong, J. Li, G. Brunner, B. Peckmann, J., 2021. A
467 novel authigenic magnetite source for sedimentary magnetization. *Geology* 49, 360–365.
468 <https://doi.org/10.1130/G48069.1>

469 Liu, Y., Lu, H., Yin, X., Ruffine, L., Çağatay, M.N., Yang, H., Chen, C., He, D., Zhu, Z., Yalamaz, B., 2019.
470 Interpretation of Late-Pleistocene/Holocene transition in the Sea of Marmara from geochemistry of bulk
471 carbonates. *Geochem. Geophys. Geosystem.* 20: 4487–4504. <https://doi.org/10.1029/2019GC008364>

472 Liu, Y., Lu, X., Çağatay, M.N., Zhang, Y., Li, Y., Peng, Y., Ruffine, L., Lu, H., 2021. The organic, inorganic and
473 isotope geochemistry of the holocene sapropel units in the sea of Marmara and their paleoceanographic
474 significance. *Mar. Petrol. Geol.* 129, 105094. <https://doi.org/10.1016/j.marpetgeo.2021.105094>

475 Luo, M., Torres, M.E., Hong, W.L., Pape, T., Fronzek, J., Kutterolf, S., Mountjoy, J.J., Orpin, A., Henkel, S.,
476 Huhn, K., Chen, D., Kasten, S., 2020. Impact of iron release by volcanic ash alteration on carbon cycling in
477 sediments of the northern Hikurangi margin. *Earth Planet. Sci. Lett.* 541, 116288.
478 <https://doi.org/10.1016/j.epsl.2020.116288>

479 Maher B.A., Thompson R., 1999. *Quaternary Climates, Environments and Magnetism.* Cambridge University
480 Press, Cambridge, UK.

481 Makaroğlu, Ö., Nowaczyk, N.R., Keriş, K.K., Çağatay, M.N., 2020. High-resolution palaeomagnetic record from
482 Sea of Marmara sediments for the last 70 ka. *Geophys. J. Int.*, 222, 2024–2039.
483 <https://doi.org/10.1093/gji/ggaa281>

484 Major, C., Ryan, W., Lericolais G., Hajdas, I., 2002. Constraints on black sea outflow to the Sea of Marmara
485 during the last glacial-interglacial transition. *Mar. Geol.* 190, 19–34. [https://doi.org/10.1016/S0025-](https://doi.org/10.1016/S0025-3227(02)00340-7)
486 [3227\(02\)00340-7](https://doi.org/10.1016/S0025-3227(02)00340-7)

487 Mazumdar, A., Peketi, A., Joao, H., Dewangan, P., Borole, D. V., Kocherla, M., 2012. Sulfidization in a shallow
488 coastal depositional setting: Diagenetic and palaeoclimatic implications. *Chem. Geol.* 322–323, 68–78.
489 <https://doi.org/10.1016/j.chemgeo.2012.06.005>

490 Merinero, R., Lunar, R., Martínez-Frías, J., Somoza, L., Díaz-del-Río, V., 2008. Iron oxyhydroxide and sulphide
491 mineralization in hydrocarbon seep-related carbonate submarine chimneys, Gulf of Cadiz (SW Iberian
492 Peninsula). *Mar. Petrol. Geol.* 25, 706–713. <https://doi.org/10.1016/j.marpetgeo.2008.03.005>

493 Murray, R.W., Leinen, M., 1996. Scavenged excess aluminum and its relationship to bulk titanium in biogenic
494 sediment from the central equatorial Pacific Ocean. *Geochim. Cosmochim. Ac.* 60, 3869–3878.
495 [https://doi.org/10.1016/0016-7037\(96\)00236-0](https://doi.org/10.1016/0016-7037(96)00236-0)

496 Musgrave, R. J., Bangs, N. L., Larrasoana, J. C., Gràcia, E., Hollamby, J. A., Vega, M. E., 2006. Rise of the base
497 of the gas hydrate zone since the last glacial recorded by rock magnetism. *Geology* 34, 117–120.
498 <https://doi.org/10.1130/G22008.1>

499 Nesbitt, H.W., Markovics, G., 1997. Weathering of granodioritic crust, long-term storage of elements in
500 weathering profiles, and petrogenesis of siliciclastic sediments. *Geochim. Cosmochim. Ac.* 61, 1653–1670.
501 [https://doi.org/10.1016/S0016-7037\(97\)00031-8](https://doi.org/10.1016/S0016-7037(97)00031-8)

502 Wei, G. Liu, Y., Li, X., Shao, L. Liang, X., 2003. Climatic impact on Al, K, Sc and Ti in marine sediments:
503 Evidence from ODP Site 1144, South China Sea. *Geochem. J.* 37: 593–602.
504 <https://doi.org/10.2343/geochemj.37.593>

505 Okay, A. İ., Kaşlılar-Özcan, A., Imren, C., Boztepe-Güney, A., Demirbağ, E., Kuşçu, İ., 2000. Active faults and
506 evolving strike-slip basins in the Marmara Sea, northwest Turkey: A multichannel seismic reflection study.
507 *Tectonophysics* 321, 189–218. [https://doi.org/10.1016/S0040-1951\(00\)00046-9](https://doi.org/10.1016/S0040-1951(00)00046-9)

508 Poulton, S., Canfield, D., 2005. Development of a sequential extraction procedure for iron: Implications for iron
509 partitioning in continentally derived particulates. *Chem Geol.* 214, 209–221.
510 <https://doi.org/10.1016/j.chemgeo.2004.09.003>

511 Pike, C.R., Roberts, A.P., Verosub, K.L., 1999. Characterizing interactions in fine magnetic particle systems
512 using first order reversal curves. *J. Appl. Phys.* 85, 6660–6667. <https://doi.org/10.1063/1.370176>

513 Roberts, A.P., 1995. Magnetic properties of sedimentary greigite (Fe₃S₄). *Earth Planet. Sci. Lett.* 134, 227–236.
514 [https://doi.org/10.1016/0012-821X\(95\)00131-U](https://doi.org/10.1016/0012-821X(95)00131-U)

515 Roberts, A.P., 2015. Magnetic mineral diagenesis. *Earth Sci. Rev.* 151, 1–47.
516 <https://doi.org/10.1016/j.earscirev.2015.09.010>

517 Roberts, A.P., Liu, Q., Rowan, C.J., Chang, L., Carvallo, C., Torrent, J., Horng, C.-S., 2006. Characterization of
518 hematite (α -Fe₂O₃), goethite (α -FeOOH), greigite (Fe₃S₄), and pyrrhotite (Fe₇S₈) using first-order reversal
519 curve diagrams. *J. Geophys. Res. Sol. Ea.* 111, B12S35. <https://doi.org/10.1029/2006JB004715>

520 Roberts, A.P., Chang, L., Heslop, D., Florindo, F., Larrasoana, J.C., 2012. Searching for single domain magnetite
521 in the “pseudo-single-domain” sedimentary haystack: Implications of biogenic magnetite preservation for
522 sediment magnetism and relative paleointensity determinations. *J. Geophys. Res. Sol. Ea.* 117, B8104.
523 <https://doi.org/10.1029/2012jb009412>

524 Roberts, A.P., Chang, L., Rowan, C.J., Horng, C.S., Florindo, F., 2011. Magnetic properties of sedimentary
525 greigite (Fe₃S₄): An update. *Rev. Geophys.* 49, RG1002. <https://doi.org/10.1029/2010RG000336>

526 Roberts, A. P., Weaver, R. (2005) Multiple mechanisms of remagnetization involving sedimentary greigite
527 (Fe₃S₄). *Earth Planet. Sci. Lett.* 231, 263–277. <https://doi.org/10.1016/j.epsl.2004.11.024>

528 Rochette P., Fillion, G., Mattéi, J.-L., Dekkers, M.J., 1990. Magnetic transition at 30–34 K in Fe₇S₈: Insight into a
529 widespread occurrence of pyrrhotite in rocks, *Earth Planet. Sci. Lett.*, 98, 319–328.
530 [https://doi.org/10.1016/0012-821X\(90\)90034-U](https://doi.org/10.1016/0012-821X(90)90034-U)

531 Ruffine, L., Cagatay, M.N., Geli, L., 2018a. Fluids and processes at the seismically active fault zone in the Sea of
532 Marmara. *Deep-Sea Res. Pt II* 153, 1–3. <https://doi.org/10.1016/j.dsr2.2018.09.011>

533 Ruffine, L., Donval, J.-P., Croguennec, C., Burnard, P., Lu, H., Germain, Y., Legoix, L.N., Bignon, L., Çağatay,
534 M.N., Marty, B., Madre, D., Pitel-Roudaut, M., Henry, P., Géli, L., 2018b. Multiple gas reservoirs are
535 responsible for the gas emissions along the Marmara fault network. *Deep-Sea Res. Pt II* 153, 48–60.
536 <https://doi.org/10.1016/j.dsr2.2017.11.011>

537 Ruffine, L., Ondreas, H., Blanc-Valleron, M.-M., Teichert, B.M.A., Scalabrin, C., Rinnert, E., Birot, D.,
538 Croguennec, C., Ponzevera, E., Pierre, C., Donval, J.-P., Alix, A.-S., Germain, Y., Bignon, L., Etoubleau, J.,
539 Caprais, J.-C., Knoery, J., Lesongeur, F., Thomas, B., Roubi, A., Legoix, L.N., Burnard, P., Chevalier, N., Lu,
540 H., Dupré, S., Fontanier, C., Dissard, D., Olgun, N., Yang, H., Strauss, H., Özaksoy, V., Perchoc, J., Podeur,

541 C., Tarditi, C., Özbeki, E., Guyader, V., Marty, B., Madre, D., Pitel-Roudaut, M., Grall, C., Embriaco, D.,
542 Polonia, A., Gasperini, L., Çağatay, M.N., Henry, P., Géli, L., 2018c. Multidisciplinary investigation on cold
543 seeps with vigorous gas emissions in the Sea of Marmara (MarsiteCruise): Strategy for site detection and
544 sampling and first scientific outcome. *Deep-Sea Res. Pt II* 153, 36–47.
545 <https://doi.org/10.1016/j.dsr2.2018.03.006>

546 Şengör, A., Görür, N., Şaroğlu, F., 1985. Strike-slip faulting and related basin formation in zones of tectonic
547 escape: Turkey as a case study. *Strike-slip deformation, basin formation, and sedimentation* 227–264.
548 <https://doi.org/10.2110/pec.85.37.0227>

549 Snowball, I., Thompson, R., 1988. The occurrence of greigite in sediments from Loch Lomond. *J. Quat.*
550 *Sci.* 3, 121–125. <https://doi.org/10.1002/jqs.3390030203>

551 Sorlien, C.C., Akhun, S.D., Seeber, L., Steckler, M.S., Shillington, D.J., Kurt, H., Çifçi, G., Poyraz, D.T., Gürçay,
552 S., Dondurur, D., 2012. Uniform basin growth over the last 500 ka, North Anatolian Fault, Marmara Sea,
553 Turkey. *Tectonophysics* 518–521, 1–16. <https://doi.org/10.1016/j.tecto.2011.10.006>

554 Tryon, M.D., Henry, Çağatay, M.N., Zitter, T.A.C. Géli, L., Gasperini, L., Burnard P., Bourlange, S., Grall, C.,
555 2010. Pore fluid chemistry of the North Anatolian Fault Zone in the Sea of Marmara: A diversity of sources
556 and processes. *Geochem. Geophys. Geosystem.* 11. <https://doi.org/10.1029/2010GC003177>

557 Vidal, L., Ménot, G., Joly, C., Bruneton, H., Rostek, F., Çağatay, M.N., Major, C., Bard, E., 2010. Hydrology in
558 the Sea of Marmara during the last 23 ka: Implications for timing of black sea connections and sapropel
559 deposition. *Paleoceanography* 25, PA1205. <https://doi.org/10.1029/2009PA001735>

560 Wilkin, R.T., Barnes, H.L., Brantley, S.L., 1996. The size distribution of framboidal pyrite in modern sediments:
561 An indicator of redox conditions. *Geochim. Cosmochim. Ac.* 60, 3897–3912. [https://doi.org/10.1016/0016-](https://doi.org/10.1016/0016-7037(96)00209-8)
562 [7037\(96\)00209-8](https://doi.org/10.1016/0016-7037(96)00209-8)

563 Yang, H., Lu, H., Ruffine, L., 2018. Geochemical characteristics of iron in sediments from the Sea of Marmara.
564 *Deep-Sea Res. Pt II* 153, 121–130. <https://doi.org/10.1016/j.dsr2.2018.01.010>

565 Yang, H., Yu, S., Lu, H., 2021. Iron-coupled anaerobic oxidation of methane in marine sediments: A Review. *J.*
566 *Mar. Sci. Eng.* 9, 875. <https://doi.org/10.3390/jmse9080875>

567 Zheng, G., Wang, X., Fortin, D., Pan, Y., Liang, M., Wu, D., Yang, R., Fan, X., Zhao, Y., 2016. Sulfur speciation
568 in marine sediments impacted by gas emissions in the northern part of the South China Sea. *Mar. Petrol. Geol.*
569 73, 181–187. <https://doi.org/10.1016/j.marpetgeo.2016.02.034>